On the structural and magnetic properties of Al-rich high entropy alloys: a joint experimental-theoretical study

OPEN ACCESS
IOP Publishing
Journal of Physics D: Applied Physics
J. Phys. D: Appl. Phys. **56** (2023) 015003 (8pp)
https://doi.org/10.1088/1361-6463/aca1ce

On the structural and magnetic properties of Al-rich high entropy alloys: a joint experimental-theoretical study

Esmat Dastanpour[1,*], Shuo Huang[2,3,*], Stephan Schönecker[1,*], Huahai Mao[1,4], Valter Ström[1], Olle Eriksson[3,5], Lajos Károly Varga[6] and Levente Vitos[1,3,6]

[1] Department of Materials Science and Engineering, KTH Royal Institute of Technology, Stockholm SE-100 44, Sweden
[2] Faculty of Materials Science and Chemistry, China University of Geosciences, Wuhan 430074, People's Republic of China
[3] Department of Physics and Astronomy, Division of Materials Theory, Uppsala University, Uppsala SE-751 20, Sweden
[4] Thermo-Calc Software AB, Råsundavägen 18, SE-169 67 Solna, Sweden
[5] School of Science and Technology, Örebro University, Örebro SE-701 82, Sweden
[6] Institute for Solid State Physics and Optics, Wigner Research Centre for Physics, Budapest H-1525, Hungary

E-mail: esmatdh@kth.se, huangshuo@cug.edu.cn and stesch@kth.se

Received 16 September 2022, revised 2 November 2022
Accepted for publication 10 November 2022
Published 29 November 2022

Abstract

The present work investigates how the vanadium (V) content in a series of $Al_{50}V_x(Cr_{0.33}Mn_{0.33}Co_{0.33})_{(50-x)}$ ($x = 12.5$, 6.5, 3.5, and 0.5 at.%) high-entropy alloys affects the local magnetic moment and magnetic transition temperature as a step towards developing high-entropy functional materials for magnetic refrigeration. This has been achieved by carrying out experimental investigations on induction melted alloys and comparison to *ab initio* and thermodynamic calculations. Structural characterization by x-ray diffraction and scanning electron microscopy indicates a dual-phase microstructure containing a disordered body-centered cubic (BCC) phase and a B2 phase with long-range order, which significantly differ in the Co and V contents. *Ab initio* calculations demonstrate a weaker magnetization and lower magnetic transition temperature (T_C) of the BCC phase in comparison with the B2 phase. We find that lower V content increases the B2 phase fraction, the saturation magnetization, and the Curie point, in line with the calculations. This trend is primarily connected with the preferential partition of V in the BCC phase, which however hinders the theoretically predicted antiferromagnetic B2 phase stabilizing effect of V. On the other hand, the chemistry-dependent properties of the ferromagnetic B2 phase suggest that a careful tuning of the composition and phase fractions can open the way towards promising high-entropy magnetic materials.

* Authors to whom any correspondence should be addressed.

Keywords: magnetic materials, high entropy alloys, *ab initio*, B2 structure, magnetic transition temperature, V content

(Some figures may appear in colour only in the online journal)

1. Introduction

High-entropy alloys (HEAs) are composed of multiple principal elements with concentrations from 5 to 35 at.% [1–4] and often contain several phases when examined at room temperature. HEAs typically crystallize in simple structures, e.g. body-centered cubic (BCC) or face-centered cubic (FCC) [5–7], although complex intermetallics and solid solution phases may be present.

Remarkable physical and chemical properties in some HEAs, such as good magnetic and electric properties, high strength and hardness, and excellent resistance to wear, corrosion, and oxidation, make them promising materials in a wide range of functional applications [8–10].

One of these applications is magnetic refrigeration, which is based on the magnetocaloric effect (MCE). The MCE exploits the temperature change in a magnetic material in response to the variation of an external magnetic field [11–14]. Magnetic refrigerant materials have received extensive attention in the recent past due to their potentially high energy efficiency and the environmentally friendly solid-state-based process in comparison with vapor compression refrigerators. A good magnetocaloric material (MCM) is characterized by large adiabatic temperature change (ΔT_{ad}), magnetic entropy change (ΔS_M), and relative cooling power (RCP), and a suitable magnetic transition temperature close to the working temperature range [15, 16]. Among the known MCMs, the B2-ordered FeRh equiatomic alloy with ΔT_{ad} of 12.9 K in 1.95 T holds a special place as a magnetic refrigerant [17]. This giant MCE in FeRh occurs by a sharp antiferromagnetic (AFM) to ferromagnetic (FM) phase transition around room temperature [18–20]. However, the raw material costs make it unlikely in a real magnetic refrigerator.

Transition metals-based HEAs with large MCE based on low-cost materials are considered to have superior commercial potential compared to systems containing e.g. Rh and also with tunable magnetic properties according to exact composition [21]. For example, Huang *et al* [13] reported that the melt-spun $Al_{0.44}Cr_{0.25}MnFeCo_{0.25}Ni_{0.2}$ alloy with the BCC structure has ΔS_M of 0.458 $Jkg^{-1}\,K^{-1}$, and RCP of 27 Jkg^{-1} at a magnetic field of ~0.82 T. Recent studies suggest that ΔS_M is larger for HEAs in the BCC structure in comparison with that in the FCC structure due to the larger coordination number of the FCC structure [22]. For example, Na *et al* [23] studied the structural and magnetocaloric properties of the AlCrFeCoNi HEA. Upon changing the Ni to Cr ratio, the structure changed from a single BCC phase for 1:1 ratio to a dual phase containing BCC and FCC phases for 1.5:0.5 ratio. They reported a peak entropy change (ΔS_M) of 0.674 $Jkg^{-1}\,K^{-1}$ for AlCrFeCoNi alloy at 290 K and 7 T and a peak entropy change (ΔS_M) of 0.277 $Jkg^{-1}\,K^{-1}$ for $AlCr_{0.5}FeCoNi_{1.5}$ alloy at 150 K and 2 T.

It is known that Al is a BCC and B2 stabilizer in HEAs [24–28]. For example, in the $Al_xCoCrNiFe$ system, above an Al content of $x = 0.5$, the fraction of BCC phase increases along with an increase in the magnetic ordering temperature and saturation magnetization. A higher fraction of Al in this alloy enables the simultaneous formation of the ordered B2 and disordered BCC phases with large differences in the magnetization and magnetic transition temperature [26]. Theoretical calculation by Li *et al* [29] suggested that the B2 structure will be formed in HEAs when the concentration of Al is larger than that of the other constituent elements combined.

In this work, we employ experiments and *ab initio* and thermodynamic calculations to investigate the phase constitution, magnetization behavior and magnetic transition temperature (T_C) of the $Al_{50}V_x(Cr_{0.33}Mn_{0.33}Co_{0.33})_{(50-x)}$ (x = 12.5, 6.5, 3.5, and 0.5 at.%) alloys. The obvious idea emerging from the *ab initio* calculations is to synthesize from inexpensive constituents a set of magnetic HEAs for MCE applications that possess the B2 structure and host AFM exchange interactions. The present experimental results indicate that V in these alloys prefers partitioning in the BCC phase, which however prevents a sizable V-level in the B2 phase and thus the AFM B2 phase cannot be stabilized. At the same time, our calculations demonstrate that the V-rich BCC phase has a smaller local magnetic moment and a lower magnetic transition temperature (T_C) compared to the V-poor B2 phase. Moreover, the T_C for the B2 phase increases with decreasing the V amount and approaches room-temperature for $x = 0.5$. This trend makes the low-V alloys candidates for room-temperature magnetic applications.

The rest of the paper is organized as follows. In section 2, we review the experimental and theoretical methodologies and explain the alloy selection. In section 3, we present all results and provide a detailed discussion.

2. Materials and methods

2.1. Experimental procedures

Samples with the nominal compositions of $Al_{50}V_x(Cr_{0.33}Mn_{0.33}Co_{0.33})_{(50-x)}$ (x = 12.5, 6.5, 3.5, and 0.5) at.% were prepared by using induction melting. The high-purity constituent elements were melted and cooled in a water-cooled copper boat. Each sample was remelted three times under ultrahigh-purity argon atmosphere to improve chemical homogeneity. For brevity, we refer to the samples as V12.5, V6.5, V3.5, and V0.5 letting the number denote the V content. These abbreviations and their full forms are used interchangeably hereafter.

The structural analysis was done by x-ray diffraction (XRD) analysis (model SIEMENS D5000) using Cu Kα radiation in $30° \leqslant 2\theta \leqslant 100°$ at a slow-scanning rate of 0.02° s^{-1}

with adopting a graphite monochromator. The phase fractions of the B2 and BCC phases were calculated by Rietveld analysis using the MAUD (material analysis using diffraction) program.

The scanning electron microscope (SEM) characterization of the materials was conducted using a Hitachi S3700N. The chemical compositions were analyzed by the SEM equipped with an energy dispersive spectrometer (EDS, Oxford Instruments, X-Max, England) operating at 15 kV. The samples were mechanically polished to a colloidal silica (0.05 μm) finish.

The hysteresis loops of the samples were determined with a vibrating sample magnetometer (VSM, EG&G model 155) under an applied field of 620 kA m^{-1} at room temperature (293 K), at ca 238–240 K (supported by 'dry ice'), and at 80 K (supported by liquid N_2). The Curie temperature of the samples was determined by AC susceptibility measurements at 181 Hz and a magnetic field of 800 A m^{-1}.

2.2. Theoretical modeling

Total energy calculations were carried out using density functional theory [30] formulated within the generalized gradient approximation [31] for the exchange-correlation functional. The Kohn–Sham equations were solved using the exact muffin-tin orbitals method [32]. The *s, p, d* and *f* orbitals were included in the muffin-tin basis set. The Green's function was calculated for 16 complex energy points around the valence states. The chemical disorder was taken into account using the coherent potential approximation [33]. The paramagnetic (PM) state was simulated by the disordered local moment (DLM) approximation [34]. The present method has been applied previously to reveal various parameters and mechanisms (e.g. order-disorder transformation) for complex multicomponent alloys [35].

Thermodynamic calculations of phase equilibria were carried out with the Thermo-Calc software [36] and the TCHEA5 database [37, 38].

2.3. Material selection

The formation of the B2 structure in HEAs is possible by using, e.g. high amounts of Al. Here, nominal compositions with 50 at.% Al were selected and Al was assumed to occupy only one sublattice of the B2 structure (nonmagnetic sublattice). Varying the concentrations of Mn, Co, and Cr (balance V) on the second sublattice (magnetic sublattice) enables tuning of the magnetic properties including magnetic ordering temperature (Curie/Néel). Mn and Co are expected to increase the Curie point, while Cr decreases it due to the AFM coupling with Mn and Co. On the other hand, previous investigations showed that vanadium acts as a stabilizer of the AFM ground state [39, 40]. Our *ab initio* calculations (not presented here) for the total energy of the FM, PM, and AFM states of the B2 structure for the $Al_{50}V_x(Cr_{0.33}Mn_{0.33}Co_{0.33})_{(50-x)}$ (x = 12.5, 6.5, 3.5, and 0.5 at.%) alloys show that the AFM state is energetically more stable in the high-V alloys, and the FM order becomes the stable magnetic state in the low-V cases. In that respect, if V is homogeneously distributed in the magnetic sublattice of the B2 phase, one could tune the competition between the magnetic states and eventually induce a metamagnetic transition similar to the one seen in FeRh.

3. Results and discussion

Figure 1 shows the XRD patterns obtained at room temperature for the $Al_{50}V_x(Cr_{0.33}Mn_{0.33}Co_{0.33})_{(50-x)}$ (x = 12.5, 6.5, 3.5, and 0.5 at.%) alloys. The diffraction peaks indicate a duplex structure consisting of BCC (space group *Im3m*) and B2 (space group *Pm3m*) phases. As seen, the peaks assigned to the B2 phase are shifted to lower angles for V3.5 and V0.5 alloys, consistent with the measured lattice constant presented in table 1. The phase fractions determined by the Rietveld method (table 1) demonstrate that the fractions of the B2 and BCC phases are dependent on the nominal V amount, i.e. the higher the V amount, the greater the BCC fraction is.

The SEM images obtained from the as-cast alloys show a mixture of dark and bright zones (figure 1). The chemical compositions extracted from SEM-EDS maps are presented in table 1. The EDS analysis can clearly identify the two zones as a Co-rich phase (bright) and a Co-poor phase (dark). For the V12.5 alloy, there is also a gray zone containing some bright precipitates, which affects the accuracy of the chemical composition determination. By correlating the peak intensities in the XRD patterns with the area fractions in the SEM images, we identify the dark zone as the BCC phase and the bright zone as the B2 phase. This is corroborated by the results of our thermodynamic calculations presented below. Decreasing the nominal amount of V to 0.5 maximizes the fraction of the B2 phase with composition $Al_{45.4}V_{0.5}Cr_{16.8}Mn_{19.5}Co_{17.4}$ (SEM-EDS), which is fairly close to the nominal composition ($Al_{50}V_{0.5}Cr_{16.5}Mn_{16.5}Co_{16.5}$).

The equilibrium phase diagram and the chemical compositions of the constitutive equilibrium phases of the V12.5 alloy (as an example) calculated by Thermo-Calc are shown in figure 2. The V12.5 alloy is predicted to solidify through a dual phase of a disordered BCC and an ordered B2 phase. At temperatures below 900 K, intermetallic compounds (Al_3Ti with Strukturbericht designation $D0_{22}$ and Al_8Mn_5 with Strukturbericht designation $D8_{10}$) are predicted to precipitate but were not observed in our experiments presumably due to the fast cooling. The corresponding chemical compositions of the B2 and BCC phases between 1000 K and 1400 K shown in figures 2(b) and (c), respectively, clarify that the main difference is the amount of Co. For example, the chemical composition of the B2 phase at 1200 K is $Al_{50}V_6Cr_5Mn_9Co_{30}$ and that of the BCC phase is $Al_{49}V_{17}Cr_{18}Mn_{15}Co_1$ (at.%). This is consistent with the SEM-EDS measurements, which determined the composition of the B2 and BCC phases as $Al_{44.7}V_{5.7}Cr_8Mn_{11.4}Co_{30.1}$ and $Al_{50.5}V_{14.6}Cr_{13.9}Mn_{14.5}Co_{6.4}$ (at.%), respectively.

Figure 3(a) presents the theoretical Curie temperatures of the B2 and BCC phases assuming the nominal composition $Al_{50}V_x(Cr_{0.33}Mn_{0.33}Co_{0.33})_{(50-x)}$ (x = 12.5, 6.5, 3.5, and 0.5) for both B2 and BCC phases as well as the experimental

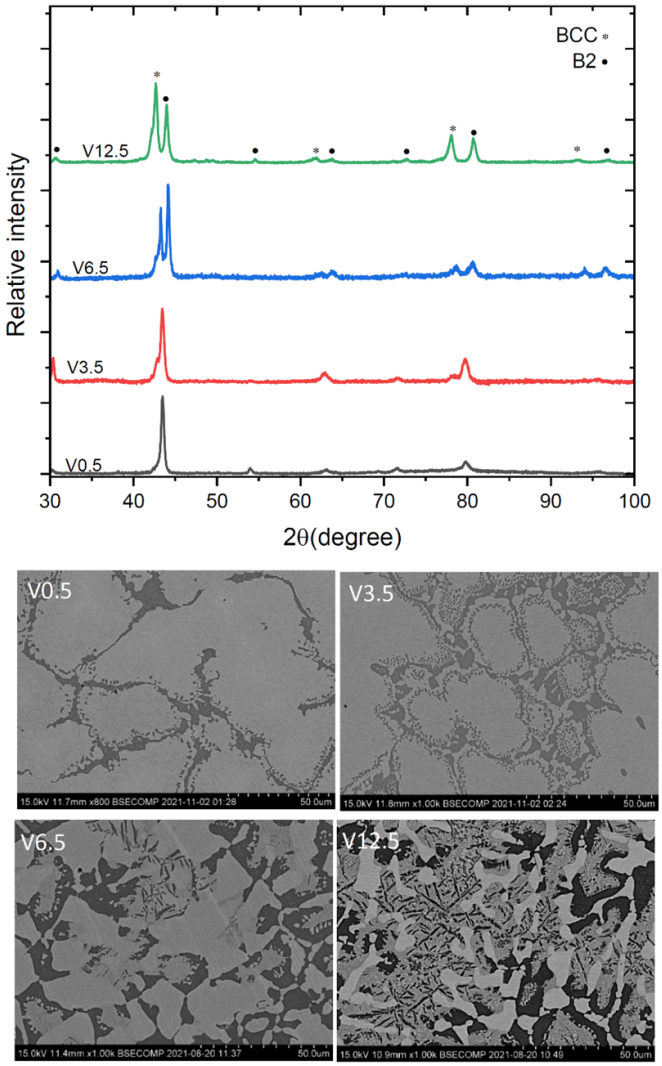

Figure 1. The XRD patterns and SEM images for the $Al_{50}V_x(Cr_{0.33}Mn_{0.33}Co_{0.33})_{(50-x)}$ ($x = 12.5$, 6.5, 3.5, and 0.5) alloys. The XRD patterns show the peaks of a BCC phase and a B2 phase. The dark and bright zones in the SEM images were identified as the BCC and B2 phases, respectively.

Curie temperatures determined from the inverse susceptibility presented in figures 3(b) and (c). In the calculations, the chemical long-range order in the B2 phase was described as Al occupying one sublattice and the remaining elements occupying the other sublattice. The Curie temperatures were estimated from $T_C = 2\Delta E/(3k_B(1-c))$, where $\Delta E = E_{PM} - E_{FM}$ is the total energy difference per atom between the PM state (DLM state) and the magnetically ordered ground state, and c the fraction of the non-spin polarized components. E_{PM} and E_{FM} were evaluated at the respective theoretical equilibrium lattice parameters [13]. From figure 3(a) it is obvious that the calculated Curie temperatures strongly depend on the chemical composition and structure. Also, the T_C of the B2 phase is significantly higher than that of the BCC phase. The T_C decreases with increasing V content in both phases. The discrepancies between the theoretical Curie temperatures and the experimental ones presented below can be ascribed, to a large extent, to the differences in the chemical compositions, the degree of B2 long-range order, and the limited accuracy of the mean field approximation to estimate the theoretical values.

The experimental T_C's were determined by assuming a Curie–Weiss behavior in the PM region, which postulates that the inverse (in phase) susceptibility is linearly dependent on the temperature. The low values of the susceptibilities for the V12.5 and V6.5 alloys in comparison with the V3.5 and V0.5 alloys confirms the weak magnetization of these samples (figures 3(b) and (c)). From the measurements we infer that the Curie temperature of the V12.5 alloy is below (<80 K) the operable range of the AC susceptometer (note that there is no experimental T_C shown in figure 3(a) for this alloy concentration). The inverse susceptibility response of the V6.5 alloy is non-linear and also suggestive of a dual-phase magnetic structure, which prohibits an accurate determination of the Curie temperature(-s). However, a naïve interpretation suggests one T_C at 247 K and another at 130 K, related to the B2 phase and the BCC phase, respectively. An enhancement of the susceptibility and magnetic transition temperature with decreasing V content can be inferred from figure 3(c). The T_C for the V3.5 alloy is 250 K for the B2 phase and 210 K for the BCC phase. For a better visualization of the T_C for the BCC phase, a magnified portion is shown as an inset. The T_C for V0.5 alloy with the B2 phase of about 97% is 275 K. Although the present alloys are not suitable for room temperature applications, from the determined trend we expect that alloys with higher critical temperatures can be achieved by e.g. omitting V. We also note that the present B2 phase do not accommodate more than approximately 6% V. The low-level of V in the B2 phase, however, cannot stabilize the expected AFM structure which would eventually open for the possibility of a metamagnetic transition according to the objective in the outset.

The calculated local magnetic moments of the BCC and B2 phases in the FM state for the $Al_{50}V_x(Cr_{0.33}Mn_{0.33}Co_{0.33})_{(50-x)}$ ($x = 12.5$, 6.5, 3.5, and 0.5) alloy assuming nominal compositions for each phase and B2 long-range order as described above are presented in figure 4(a). It is demonstrated that the local magnetic moment per atom in the B2 phase is larger than in the BCC phase in all the alloys, corresponding to a higher magnetization per atom of the B2 phase. For example, the local magnetic moment for the B2 and BCC phases in V0.5 alloy are 0.73 μ_B/atom and 0.43 μ_B/atom, respectively. The effective magnetic moment of the B2 + BCC composite, calculated by averaging the moments of the BCC and B2 phases weighted by their experimental phase fractions (table 1), shows stronger magnetization by decreasing the nominal V content. The highest effective magnetic moment (0.73 μ_B/atom) occurs for V0.5 alloy and is close to the local magnetic moment per atom of the B2 phase due to the high volume fraction of the B2 phase (96.9%) in this alloy.

The measured hysteresis loops at room temperature shown in figure 4(b) demonstrate that the PM contribution is dominant at high magnetic fields for the two alloy cases with $x = 12.5$

Table 1. The chemical compositions, lattice constants, and phase fractions based on the XRD patterns and SEM analysis for the $Al_{50}V_x(Cr_{0.33}Mn_{0.33}Co_{0.33})_{(50-x)}$ ($x = 12.5$, 6.5, 3.5, and 0.5) alloys.

Alloys	Structure	Lattice constant (Å)	Chemical composition	Phase fraction (%V)
V12.5	Bright: B2	2.910	Al44.7V5.7Cr8.0Mn11.4Co30.1	53.1
	Dark: BCC	2.990	Al50.5V14.6Cr13.9Mn14.5Co6.4	46.9
	Gray	—	Al43.5V12Cr11.9Mn12.7Co19.9	—
V6.5	Bright: B2	2.902	Al46.1V4.4Cr12.6Mn13.4Co23.4	64.9
	Dark: BCC	2.958	Al53.2V7.8Cr16.8Mn16.5Co5.7	35.1
V3.5	Bright: B2	2.942	Al45.2V3.4Cr15.6Mn18.0Co17.8	83.2
	Dark: BCC	2.984	Al51.6V4.3Cr17.4Mn21.4Co5.3	16.8
V0.5	Bright: B2	2.943	Al45.4V0.5Cr16.8Mn19.5Co17.4	96.9
	Dark: BCC	2.984	Al48.1V0.8Cr21.5Mn21.9Co4.6	3.1

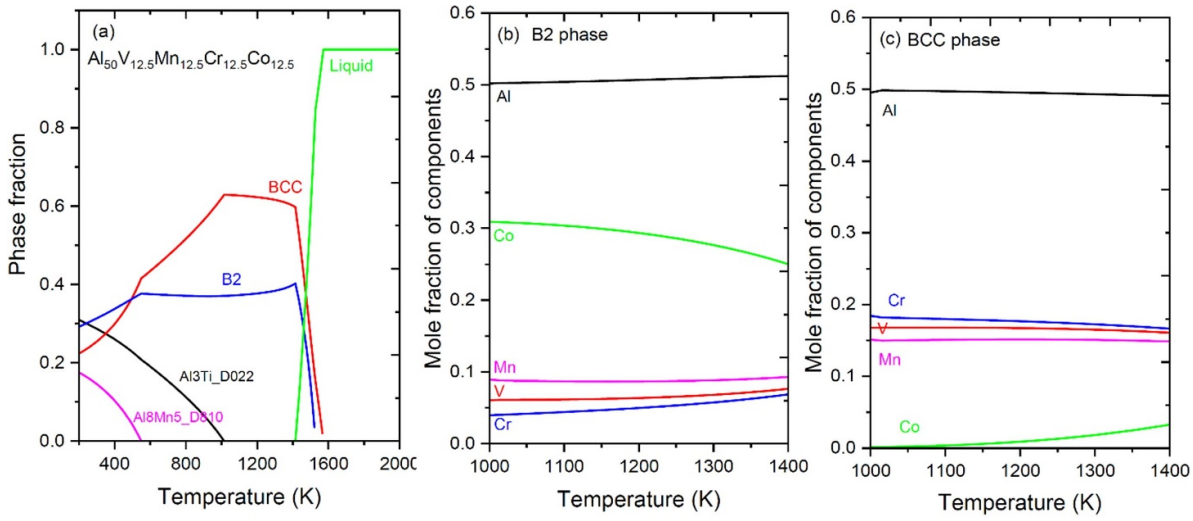

Figure 2. (a) Calculated equilibrium phase fractions with the Thermo-Calc software, and (b), (c) the chemical compositions of the constitutive equilibrium B2 and BCC phases for V12.5 alloy between 1000 K and 1400 K. A dual phase containing BCC and B2 phases may be expected in the as-cast V12.5 alloy. The main difference in the chemical composition between the BCC and B2 phases is the fraction of Co, which tends to accumulate in the B2 phase.

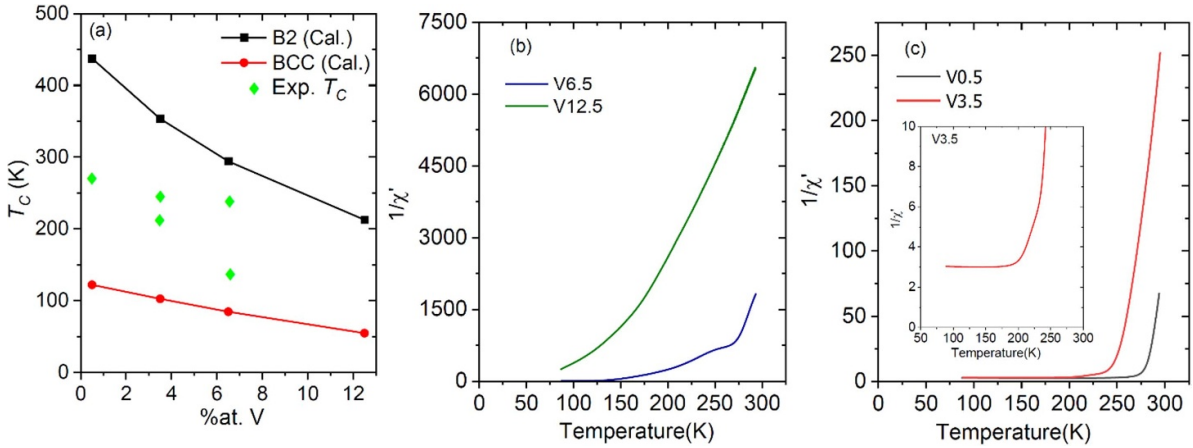

Figure 3. (a) Calculated (Cal.) Curie temperatures for the B2 and BCC phases *vs.* V content assuming nominal and homogeneous alloy compositions. The experimental (Exp.) Curie temperatures determined from (b) and (c) are presented for comparison. Panels (b) and (c) show the inverse susceptibility *vs*. temperature for $Al_{50}V_x(Cr_{0.33}Mn_{0.33}Co_{0.33})_{(50-x)}$ ($x = 12.5$, 6.5, 3.5, and 0.5) alloys, which allows the determination of the Curie point by assuming a Curie–Weiss behavior. The insert in (c) is a magnification of inverse susceptibility for V3.5 alloy.

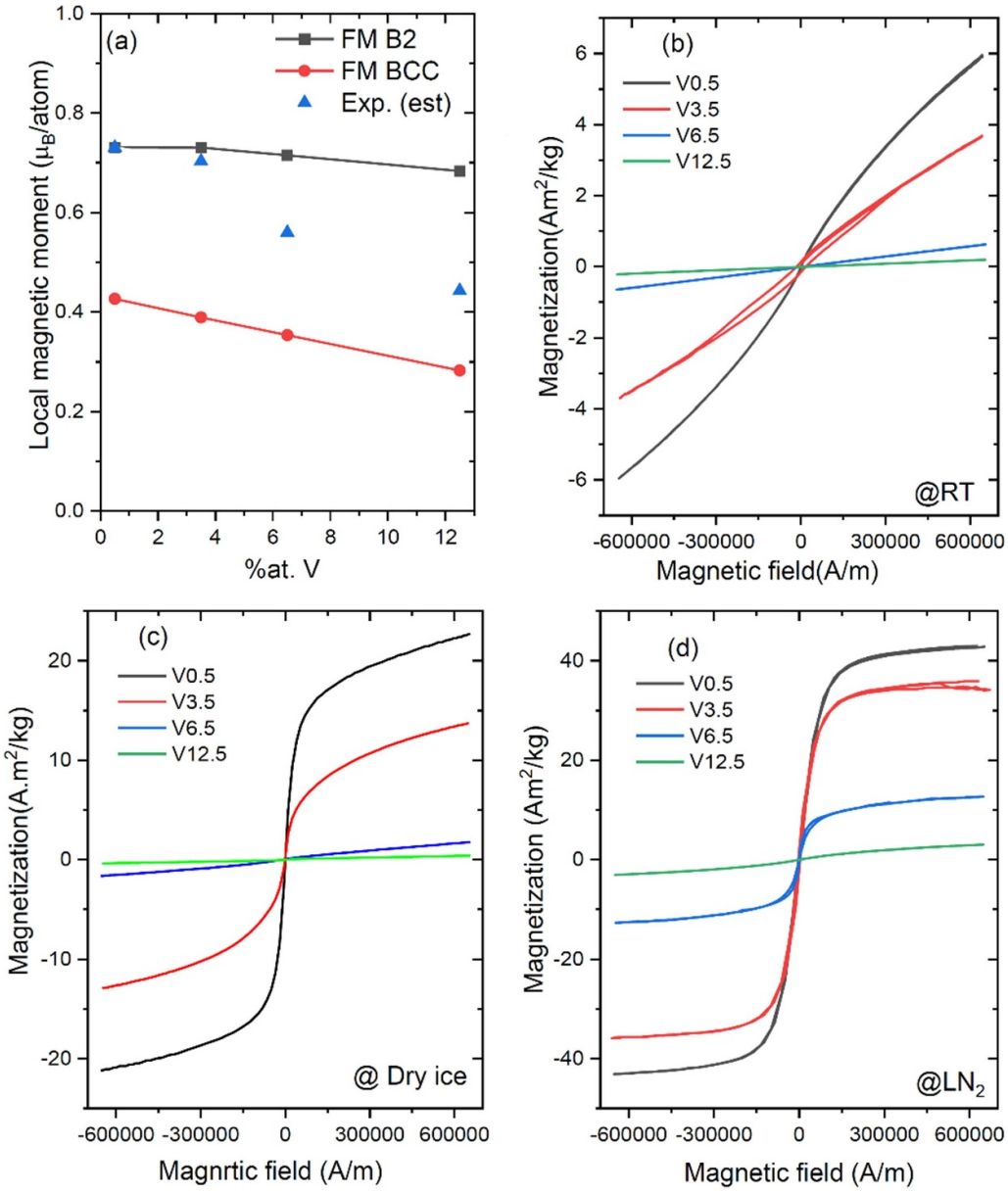

Figure 4. (a) The calculated local magnetic moments of the BCC and B2 phases in the FM state and estimated experimental numbers (Exp. (est)) for the BCC + B2 composite (for details, see main text). The hysteresis loops for the $Al_{50}V_x(Cr_{0.33}Mn_{0.33}Co_{0.33})_{(50-x)}$ ($x = 12.5$, 6.5, 3.5, and 0.5) alloys under a maximum magnetic field of 620 kA m^{-1} at room temperature (RT) (b), at dry ice condition (c), and at liquid nitrogen (LN_2) temperature (d).

and 6.5. The FM contribution increases with decreasing V content, e.g. the magnetization at the maximum magnetic field for V12.5 is about 0.2 Am^2 kg^{-1}, while it increases to about 6 Am^2 kg^{-1} for V0.5 alloy. This change is consistent with the above *ab initio* results for the local magnetic moments. The hysteresis loops measured in dry ice and at the boiling point of liquid nitrogen shown in figures 4(c) and (d), respectively, present different magnetization behaviors. The *M-H* plots for the V0.5 and V3.5 samples at dry ice condition signal the proximity to their Curie points, whereas their magnetization curves saturate at liquid nitrogen condition. The PM state of the V12.5 alloy at liquid nitrogen condition affirms the low T_C of this alloy consistent with the susceptibility measurement (figure 3(b)).

4. Conclusions

We have investigated the effect of V on the structural and magnetic properties for a series of $Al_{50}V_x(Cr_{0.33}Mn_{0.33}Co_{0.33})_{(50-x)}$ ($x = 12.5$, 6.5, 3.5, and 0.5) HEAs by using experiments, and *ab initio* and thermodynamic calculations. The main findings are summarized as follows:

- The XRD analysis and SEM-EDS observations indicate a duplex structure containing BCC (Co-poor) and B2 (Co-rich) phases, which is consistent with the Thermo-Calc results.
- Decreasing the V content stimulates formation of a single B2 phase.

- The V content in the B2 phase is not sufficiently high to stabilize the AFM state. In fact, the B2 phase does not accept more than approximately 6 at.% V.
- The calculated T_C's for the BCC and B2 phases demonstrate tunable T_C with changing the fraction of V content. The experimental T_C increases with decreasing V, in line with calculations.
- The BCC phase has a lower calculated magnetization in the FM state than the B2 phase. At the boiling point of liquid nitrogen, the V0.5 and V3.5 alloys are in the FM state, while the V6.5 and V12.5 alloys are PM.

Data availability statement

No new data were created or analysed in this study.

Acknowledgments

This work was supported by the Swedish Foundation for Strategic Research, the Swedish Research Council (Grant Agreement Nos. 2017-06474 and 2019-04971), the Sweden's Innovation Agency (VINNOVA Grant No. 2019-05111), the Carl Tryggers Foundation (Grant Agreement Nos. 19:325 and 20:474), and the Hungarian Scientific Research Fund (OTKA No. 128229).

ORCID iDs

Esmat Dastanpour https://orcid.org/0000-0003-1296-2728
Shuo Huang https://orcid.org/0000-0003-4165-6690
Stephan Schönecker https://orcid.org/0000-0001-9317-6205
Huahai Mao https://orcid.org/0000-0002-8493-9802
Valter Ström https://orcid.org/0000-0003-2170-0076
Olle Eriksson https://orcid.org/0000-0001-5111-1374
Lajos Károly Varga https://orcid.org/0000-0001-8068-0197
Levente Vitos https://orcid.org/0000-0003-2832-3293

References

[1] Yeh J W, Chen S K, Lin S J, Gan J Y, Chin T S, Shun T T, Tsau C H and Chang S Y 2004 Nanostructured high-entropy alloys with multiple principal elements: novel alloy design concepts and outcomes *Adv. Eng. Mater.* **6** 299–303
[2] Cantor B, Chang I T H, Knight P and Vincent A J B 2004 Microstructural development in equiatomic multicomponent alloys *Mater. Sci. Eng.* A **375–377** 213–8
[3] George E P, Raabe D and Ritchie R O 2019 High-entropy alloys *Nat. Rev. Mater.* **4** 515–34
[4] Gao M C, Miracle D B, Maurice D, Yan X, Zhang Y and Hawk J A 2018 High-entropy functional materials *J. Mater. Res.* **33** 3138–55
[5] Diao H Y, Feng R, Dahmen K A and Liaw P K 2017 Fundamental deformation behavior in high-entropy alloys: an overview *Curr. Opin. Solid State Mater. Sci.* **21** 252–66
[6] Lu Y *et al* 2014 A promising new class of high-temperature alloys: eutectic high-entropy alloys *Sci. Rep.* **4** 1–5
[7] Shi P, Ren W, Zheng T, Ren Z, Hou X, Peng J, Hu P, Gao Y, Zhong Y and Liaw P K 2019 Enhanced strength–ductility synergy in ultrafine-grained eutectic high-entropy alloys by inheriting microstructural lamellae *Nat. Commun.* **10** 1–8
[8] Miracle D B and Senkov O N 2017 A critical review of high entropy alloys and related concepts *Acta Mater.* **122** 448–511
[9] Ye Y F, Wang Q, Lu J, Liu C T and Yang Y 2016 High-entropy alloy: challenges and prospects *Mater. Today* **19** 349–62
[10] Zhang Y, Zuo T T, Tang Z, Gao M C, Dahmen K A, Liaw P K and Lu Z P 2014 Microstructures and properties of high-entropy alloys *Prog. Mater. Sci.* **61** 1–93
[11] Huang S, Dong Z, Mu W, Ström V, Chai G and Vitos L 2020 Thermo-elastic properties of bcc Mn-rich high-entropy alloy *Appl. Phys. Lett.* **117** 1–6
[12] Dong Z, Huang S, Ström V, Chai G, Varga L K, Eriksson O and Vitos L 2021 $MnxCr_{0.3}Fe_{0.5}Co_{0.2}Ni_{0.5}Al_{0.3}$ high entropy alloys for magnetocaloric refrigeration near room temperature *J. Mater. Sci. Technol.* **79** 15–20
[13] Huang S, Dong Z, Mu W, Ström V, Chai G, Varga L K, Eriksson O and Vitos L 2021 Magnetocaloric properties of melt-spun MnFe-rich high-entropy alloy *Appl. Phys. Lett.* **119** 1–6
[14] Kim Y, Kim E J, Choi K, Han W B, Kim H S, Shon Y and Yoon C S 2014 Room-temperature magnetocaloric effect of Ni-Co-Mn-Al Heusler alloys *J. Alloys Compd.* **616** 66–70
[15] Franco V, Blázquez J S, Ingale B and Conde A 2012 The magnetocaloric effect and magnetic refrigeration near room temperature: materials and models *Annu. Rev. Mater. Res.* **42** 305–42
[16] Phan M H and Yu S C 2007 Review of the magnetocaloric effect in manganite materials *J. Magn. Magn. Mater.* **308** 325–40
[17] Chirkova A, Skokov K P, Schultz L, Baranov N V, Gutfleisch O and Woodcock T G 2016 Giant adiabatic temperature change in FeRh alloys evidenced by direct measurements under cyclic conditions *Acta Mater.* **106** 15–21
[18] Scheibel F, Gottschall T, Taubel A, Fries M, Wende H, Farle M, Acet M and Gutfleisch O 2018 Hysteresis design of magnetocaloric materials—from basic mechanisms to applications *Energy Technol.* **6** 1397–428
[19] Navarro E, Multigner M, Yavari A R and Hernando A 1996 The spin glass state of metastable fcc FeRh *Eur. Lett.* **35** 307–11
[20] Vieira R M, Eriksson O, Bergman A and Herper H C 2021 High-throughput compatible approach for entropy estimation in magnetocaloric materials: feRh as a test case *J. Alloys Compd.* **857** 1–11
[21] Belyea D D, Lucas M S, Michel E, Horwath J and Miller C W 2015 Tunable magnetocaloric effect in transition metal alloys *Sci. Rep.* **5** 1–8
[22] Alzate-Cardona J D, Salcedo-Gallo J S, Rodríguez-Patiño D F, Acosta-Medina C D and Restrepo-Parra E 2019 Unveiling a scaling and universal behavior for the magnetocaloric effect in cubic crystal structures: a monte carlo simulation *Sci. Rep.* **9** 1–7
[23] Na S M, Lambert P K, Kim H, Paglione J and Jones N J 2019 Thermomagnetic properties and magnetocaloric effect of FeCoNiCrAl-type high-entropy alloys *AIP Adv.* **9** 1–6
[24] Hillel G, Natovitz L, Salhov S, Haroush S, Pinkas M and Meshi L 2020 Understanding the role of the constituting elements of the alcocrfeni high entropy alloy through the investigation of quaternary alloys *Metals* **10** 1–11
[25] Santodonato L J, Liaw P K, Unocic R R, Bei H and Morris J R 2018 Predictive multiphase evolution in Al-containing high-entropy alloys *Nat. Commun.* **9** 1–10

[26] Cieslak J, Tobola J, Berent K and Marciszko M 2018 Phase composition of Al x FeNiCrCo high entropy alloys prepared by sintering and arc-melting methods *J. Alloys Compd.* **740** 264–72
[27] Jasiewicz K, Cieslak J, Kaprzyk S and Tobola J 2015 Relative crystal stability of AlxFeNiCrCo high entropy alloys from XRD analysis and formation energy calculation *J. Alloys Compd.* **648** 307–12
[28] Asadikiya M, Yang S, Zhang Y, Lemay C, Apelian D and Zhong Y 2021 A review of the design of high-entropy aluminum alloys: a pathway for novel Al alloys *J. Mater. Sci.* **56** 12093–110
[29] Li C, Zhao M, Li J C and Jiang Q 2008 B2 structure of high-entropy alloys with addition of Al *J. Appl. Phys.* **104** 1–6
[30] Hohenberg P and Kohn W 1964 Inhomogenous electron gas *Phys. Rev.* B **136** 864–71
[31] Perdew J P, Burke K and Ernzerhof M 1996 Generalized gradient approximation made simple *Phys. Rev. Lett.* **77** 3865–8
[32] Vitos L 2007 *Computational Quantum Mechanics for Materials Engineers* (London: Springer)
[33] Soven P 1967 Coherent-potential model of substitutional disordered alloys *Phys. Rev.* **156** 809–13
[34] Gyorffy B L, Pindor A J, Staunton J, Stocks G M and Winter H 1985 A first-principles theory of ferromagnetic phase transitions in metals *J. Phys. F: Met. Phys.* **15** 1337–86
[35] Huang S, Li W, Eriksson O and Vitos L 2020 Chemical ordering controlled thermo-elasticity of $AlTiVCr_{1-x}Nb_x$ high-entropy alloys *Acta Mater.* **199** 53–62
[36] Andersson J O, Helander T, Höglund L, Shi P and Sundman B 2002 THERMO-CALC & DICTRA, computational tools for materials science *Calphad* **26** 273–312
[37] Chen H L, Mao H and Chen Q 2018 Database development and Calphad calculations for high entropy alloys: challenges, strategies, and tips *Mater. Chem. Phys.* **210** 279–90
[38] Mao H, Chen H L and Chen Q 2017 TCHEA1: a thermodynamic database not limited for "high entropy" alloys *J. Phase Equilib. Diffus.* **38** 353–68
[39] Freitas D *et al* 2013 Antiferromagnetism and ferromagnetism in layered 1T-$CrSe_2$ with V and Ti replacements *Phys. Rev.* B **87** 1–9
[40] Vega A, Rubio A, Balbas L C, Dorantes-Davila J, Bouarab S, Demangeat C, Mokrani A and Dreysse H 1991 Antiferromagnetic interlayer coupling in Fe/V and Fe/Cr *J. Appl. Phys.* **69** 4544–6